

## Simulation of Thermo-fluid Interactions in Cryogenic Stage Turbine Startup System Using AUSM+-UP-based Higher-order Accurate Flow Solver

Praveen Nair<sup>1</sup>, Jayachandran T.<sup>1</sup>, Balachandra Puranik<sup>2</sup>, and Upendra V. Bhandarkar<sup>2</sup>

<sup>1</sup>Vikram Sarabhai Space Centre, Thiruvananthapuram-695 022

<sup>2</sup>Indian Institute of Technology Bombay, Mumbai-400 076

### ABSTRACT

High-speed turbines are used in upper stage liquid engines of launch vehicles and the most common ones include LH2 and LOX turbines used in the cryogenic stages. The main constraints in the design of turbine system for a liquid engine are thermal loads, mass flow and pressure drops in various systems ahead of the turbine inlet. The temperature of the combustion products/gases reaching the turbine blades must be well below the melting point of the turbine blade material and the mass flow rate must be sufficient to generate the required power. Turbine can be started in two ways, by generating gases using a solid propellant-based spinner motor, and using compressed gases stored in gas bottles. The first method involves design challenges but requires less space and weight. On the other hand, second method is simple but requires more space. Because of the space and weight constraints associated with the upper stages, first method is preferred and discussed in this paper. It consists of a solid propellant-based spinner motor with a convergent-divergent nozzle, a guiding duct connecting nozzle exit, and the turbine inlet manifold in the form of a torroid with nozzle block having 39 guiding nozzles. The combustion products generated by the spinner motor are guided to the manifold through the guiding duct. Inlet manifold acts as a reservoir and supplies hot gases uniformly to the turbine through 39 nozzles. This study addresses the role of computational fluid dynamics in the design of turbine startup system using unstructured cell-centered AUSM+-UP-based finite volume solver with the two-equation turbulence model. The flow and the thermal characteristics of the solid motor with a convergent-divergent nozzle were studied to evaluate the gas temperature, operating pressure, and flow velocities. The guiding duct along with the inlet manifold was analysed separately to find the drop in temperature and pressure within the system. From the simulation results, the mass flow through each guiding nozzle, and hence, energy available could be evaluated to ensure proper functioning of the turbine.

**Keywords:** Unstructured meshes, solid motor, AUSM+-UP based finite volume solver, turbine inlet manifold, least square reconstruction, solution mapped, flux limiters.

### NOMENCLATURE

$C_p$	Specific heat at constant pressure	$T, T_0$	Static temperature, Stagnation temperature
$C_\mu, C_\epsilon$	Closure coefficient	$t$	Time
$E$	Total energy	$t$	Turbulent
$E_{ij}$	Deformation tensor	$U$	Vector of conservative variables
$E_{ff}$	Effective value	$V$	Volume of the control volume
$F, G$	Flux vectors	$u$	Velocity in $x$ direction
$i, j$	Cell and neighbour index	$v$	Velocity in $y$ direction
$K$	Thermal conductivity	$v_r$	Velocity in radial direction
$l$	Laminar	$x, y$	Cartesian coordinates
$M$	Mach number	$Y_i$	Mass fraction
$N_n$	Number of neighbours	$\epsilon$	Kinetic energy dissipation rate
$n$	Order of accuracy	$\epsilon_{ij}$	Error in reconstruction
$P, P_0$	Static pressure, Stagnation pressure	$F$	Primitive variable
$P_r$	Prandtl Number	$\kappa$	Kinetic energy of turbulence
$Q$	Heat flux	$\mu$	Dynamic viscosity
$R$	Universal gas constant	$\rho$	Density
$R$	Residue	$\sigma$	Shear stress
$r$	Radial distance	$\omega$	Geometric weights
$S$	Source term	$\omega_s$	Solution weights

Received 10 June 2008

**1. INTRODUCTION**

A detailed 3-D simulation of internal flow field of a turbine startup system provides the designer with information necessary for selecting the material and propellant, calculating hardware thickness, arriving at appropriate geometry for optimum design, and predicting the turbine performance. The turbine startup system consists of a solid propellant-based spinner motor with a convergent-divergent nozzle, a guiding duct connecting nozzle exit, and the turbine inlet manifold in the form of a torroid with nozzle block having 39 guiding nozzles. Solid propellants used in spinner motors must generate required quantity of combustion products with minimum particulate content<sup>1,2</sup> which otherwise can damage turbine blades. The temperature of the combustion products must be as low as possible to protect the turbine blades whereas its  $C_p$  value must be as high as possible to minimise the propellant loading. Hence a trade-off is required between the above two requirements. The guiding duct, which connects the solid motor nozzle with the turbine inlet housing, must be designed so as to ensure minimum pressure loss and required temperature at duct exit. The geometry of the duct must prevent direct hit of the hot gases which otherwise would result in local thermal stress. The inlet manifold should act as a fluid reservoir within a short span of time, thereby ensuring uniform flow through guiding nozzles. The guiding nozzle contour must ensure that the flow is free from shocks and other disturbances. The role of CFD tools for meeting the above design requirements can be summarised as follows:

- Prediction and simulations of flow and thermal characteristics of the turbine startup motor to meet the thermal and mass flow requirements.
- Design of convergent-divergent nozzle for the turbine startup motor.
- Positioning of the motor over the duct to satisfy thermal and flow constraints.
- Analysis of flow within the inlet manifold to find mass flow through each of the guiding nozzle and net pressure drop in the manifold.
- Integrated analysis of solid motor with C-D nozzle, duct and inlet manifold with guiding nozzles to find net pressure and mass flow rate to the turbine and the thermal load which acts on the turbine blades.

For the entire CFD simulations and predictions, unstructured cell-centered AUSM+-UP-based finite volume solver was used. Heat transfer was predicted using appropriate engineering correlations.

**2. GOVERNING EQUATIONS**

The conservation form of equations, which govern 2-D/axisymmetric turbulent compressible flow can be expressed in a generic form as<sup>3,4</sup>

$$\frac{\partial U}{\partial t} + \frac{\partial F}{\partial x} + \frac{1}{r^m} \frac{\partial(r^m G)}{\partial y} = S \tag{1}$$

where  $m = 0$  for 2-D and  $m = 1$  for axisymmetric problems

$$U = \begin{bmatrix} \rho \\ \rho u \\ \rho v_r \\ \rho E \\ \rho \kappa \\ \rho \varepsilon \\ \rho Y_i \end{bmatrix}, F = \begin{bmatrix} \rho u \\ \rho u^2 + \sigma_{xx} \\ \rho uv_r + \sigma_{xr} \\ (\rho E + \sigma_{xx})u + \sigma_{xr}v_r - K_{eff} \frac{\partial T}{\partial x} \\ \rho u \kappa - \mu_{\kappa} \frac{\partial \kappa}{\partial x} \\ \rho u \varepsilon - \mu_{\varepsilon} \frac{\partial \varepsilon}{\partial x} \\ \rho u Y_i - D' \frac{\partial Y_i}{\partial x} \end{bmatrix}$$

$$G = \begin{bmatrix} \rho v_r \\ \rho uv_r + \sigma_{rx} \\ \rho v_r^2 + \sigma_{rr} \\ (\rho E + \sigma_{rr})v_r + \sigma_{rx}u - K_{eff} \frac{\partial T}{\partial r} \\ \rho v_r \kappa - \mu_{\kappa} \frac{\partial \kappa}{\partial r} \\ \rho v_r \varepsilon - \mu_{\varepsilon} \frac{\partial \varepsilon}{\partial r} \\ \rho u Y_i - D' \frac{\partial Y_i}{\partial y} \end{bmatrix} \text{ and } S = \begin{bmatrix} 0 \\ 0 \\ \frac{m}{r}(P + \sigma_{\theta\theta}) \\ 0 \\ H_{\kappa} \\ H_{\varepsilon} \\ \omega \end{bmatrix}$$

Here,

$$\sigma_{xx} = P + \frac{2}{3} \rho \kappa - \mu_{eff} \left[ 2 \frac{\partial u}{\partial x} - \frac{2}{3} \left( \frac{\partial u}{\partial x} + \frac{1}{r} \frac{\partial r v_r}{\partial r} \right) \right]$$

$$\sigma_{xr} = \sigma_{rx} = -\mu_{eff} \left[ \frac{\partial u}{\partial r} + \frac{\partial v_r}{\partial x} \right]$$

$$\sigma_{rr} = P + \frac{2}{3} \rho \kappa - \mu_{eff} \left[ 2 \frac{\partial v_r}{\partial r} - \frac{2}{3} \left( \frac{\partial u}{\partial x} + \frac{1}{r} \frac{\partial r v_r}{\partial r} \right) \right]$$

$$\sigma_{\theta\theta} = -\mu_{eff} \left[ 2 \frac{v_r}{r} - \frac{2}{3} \left( \frac{\partial u}{\partial x} + \frac{1}{r} \frac{\partial r v_r}{\partial r} \right) \right]$$

In the above versions of formulations, the effective viscosity of the flow field is

$$\mu_{eff} = \mu_l + \mu_t \tag{2}$$

From Sutherland's law, laminar viscosity can be evaluated as

$$\mu_l = 1.458 \times 10^{-6} \frac{T^{1.5}}{T + 110.4}$$

and  $\mu_t$  is found from turbulence model. The effective thermal conductivity is

$$K_{eff} = K_l + K_t \tag{3}$$

in which the laminar and turbulent conductivities are

$$k_l = \frac{\mu_l C_p}{Pr} \text{ and } k_t = \frac{\mu_t C_p}{Pr_t}$$

For the present analysis, modified  $\kappa$ - $\varepsilon$  model called

Renormalisation Group (RNG) model was used. Yakhot<sup>5</sup>, *et al.* had proposed this model, which systematically removes all the small scales of turbulence motion from the governing equation by expressing their effects in terms of large scales and a modified viscosity. Following are the two equations related to RNG model.

$$\frac{\partial(\rho\kappa)}{\partial t} + \text{div}(\rho\kappa U) = \text{div}[\alpha_\kappa \mu_{eff} \text{grad}\kappa] + H_\kappa \quad (4)$$

$$\frac{\partial(\rho\varepsilon)}{\partial t} + \text{div}(\rho\varepsilon U) = \text{div}[\alpha_\varepsilon \mu_{eff} \text{grad}\varepsilon] + H_\varepsilon \quad (5)$$

Here, the turbulence source terms are obtained as

$$H_\kappa = 2\mu_t E_{ij} - \rho\varepsilon \quad \text{and} \quad H_\varepsilon = C_{1\varepsilon}^* \frac{\varepsilon}{\kappa} 2\mu_t E_{ij} E_{ij} - C_{2\varepsilon} \rho \frac{\varepsilon^2}{\kappa}$$

Turbulent viscosity is defined as

$$\mu_t = \rho C_\mu \frac{\kappa^2}{\varepsilon}$$

Closure coefficients are evaluated as

$$C_\mu = 0.0845, \quad \alpha_\kappa = \alpha_\varepsilon = 1.39, \quad C_{1\varepsilon} = 1.42, \quad C_{2\varepsilon} = 1.68$$

$$\eta = \sqrt{(2E_{ij} E_{ij})^{k/2}} \quad \text{and} \quad C_{1\varepsilon}^* = C_{1\varepsilon} - \frac{\eta(1 - \eta/\eta_0)}{1 + \beta\eta^3}$$

$$\eta_0 = 4.377, \quad \beta = 0.012$$

All other parameters are explicitly computed as part of the RNG calculations.

### 3. SCHEMES, MODELS AND FLOWCHARTS

#### 3.1 Finite Volume Formulation And Time Integration

The finite volume method is compatible enough to handle unstructured grids, if information regarding the neighboring elements is supplied. In this analysis, the domain was divided into quadrilateral control volumes.

The basic conservation equation is

$$\frac{\partial U}{\partial t} + \nabla \cdot F - S = 0 \quad (6)$$

Integrating this equation,

$$\int \left( \frac{\partial U}{\partial t} + \nabla \cdot F - S \right) d\Omega = 0 \quad (7)$$

$$\int \frac{\partial U}{\partial t} d\Omega + \int \nabla \cdot F d\Omega - \int S d\Omega = 0 \quad (8)$$

Applying Green's theorem

$$\int_\Omega \frac{\partial U}{\partial t} d\Omega + \int_\Gamma F n d\Gamma - \int_\Omega S d\Omega = 0 \quad (9)$$

where  $\Gamma$  and  $\Omega$  are respectively the surface area and volume of the cell. The above equation can be rewritten as

$$\frac{dU_i}{dt} V_i + \sum_{\text{faces}} F \cdot ds - S_i V_i = 0 \quad (10)$$

Here  $V_i$  is the cell volume and  $ds$  is the area of elemental sides.

For the simple explicit scheme the time stepping using Runge-Kutta method are

$$\begin{aligned} U_i^{(0)} &= U_i^{(n)} \\ U_i^{(1)} &= U_i^{(0)} - \alpha_1 \frac{\Delta t_i}{V_i} (R_i^{(0)}) \\ U_i^{(2)} &= U_i^{(0)} - \alpha_2 \frac{\Delta t_i}{V_i} (R_i^{(1)}) \\ U_i^{(3)} &= U_i^{(0)} - \alpha_3 \frac{\Delta t_i}{V_i} (R_i^{(2)}) \\ U_i^{n+1} &= U_i^n + U_i^{(3)} \end{aligned} \quad (11)$$

where the superscripts  $n$  and  $n+1$  indicate the current and the next time steps. The values of coefficients in Runge-Kutta integration procedure are  $\alpha_1=0.6$ ,  $\alpha_2=0.6$  and  $\alpha_3=1.0$ . This method is only conditionally stable, as it is an explicit method. Local time stepping was employed for accelerating convergence. Thus, each control volume can march with its own maximum allowable time step specified by the explicit stability criteria given by

$$\Delta t_i \leq \frac{\Delta l_i}{q_i + c} \quad (12)$$

where  $q_i$  is the magnitude of fluid velocity of  $i^{\text{th}}$  cell, given by

$$q_i = \sqrt{u_i^2 + v_i^2}$$

and  $c = \sqrt{\gamma RT}$ , the sound velocity and  $\Delta l_i$  is the characteristic dimension of the quadrilateral element. Now the time step of the explicit solution procedure is given by

$$\Delta t_i = \text{CFL} \times \frac{\Delta l_i}{q_i + c} \quad (13)$$

where CFL is the Courant, Friedrichs, and Lewis number, respectively.

#### 3.2 Viscous flux Evaluation

In the case of Navier-Stokes equations, the viscous flux components contain derivatives of  $u$ ,  $v$ , and  $T$  that are evaluated along the edge. For example, to calculate the derivatives of  $u$  along side  $n3-n4$ , a pseudo cell ABCD is considered as shown in Fig. 1 and the derivative is evaluated using the expression:

$$\left( \frac{\partial u}{\partial x} \right)_{n3-n4} = \frac{(u_A - u_C)(y_B - y_D) - (u_B - u_D)(y_A - y_C)}{(x_A - x_C)(y_B - y_D) - (x_B - x_D)(y_A - y_C)} \quad (14)$$

Nodal values of the flow parameters can be evaluated using higher-order reconstruction scheme described in Section 3.4. The same procedure was adopted for the derivatives across other sides

#### 3.3 Inviscid Flux Evaluation using AUSM+-UP

In upwind schemes, the discretisation of the equations on a mesh is performed according to the direction of propagation of information on that mesh, thereby incorporating the physical phenomena into the discretisation schemes.

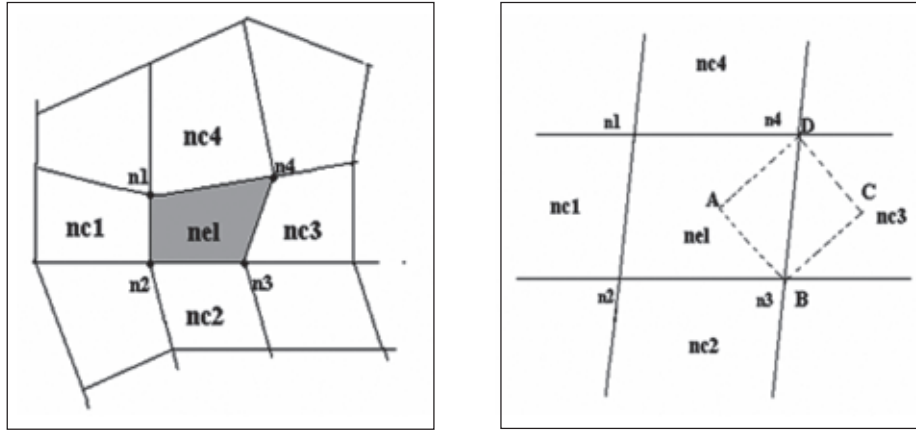


Figure 1. Finite Volume connectivity and pseudo control volume details.

There were essentially two approaches for identifying the upwind directions, namely the Godunov approach and the flux vector splitting (FVS) approach<sup>6</sup>. These two approaches are respectively referred to as Riemann approach and the Boltzmann approach. The respective numerical methods derived from these two approaches are referred to as flux difference splitting (FDS) methods and flux vector splitting (FVS) methods. The Basic implementation of these two methods is given by Harten , Lax and Van Leer<sup>7</sup>.

3.3.1 Literature Comments on Flux Vector Splitting and Flux Difference Splitting

Flux vector splitting, such as Steger-Warming or Van Leer’s has advantages in view of robustness and efficiency. It can be proved that these schemes are positively conservative under a CFL-like condition<sup>10</sup>, which is desirable for simulating high-speed flows involving strong shocks and expansions. However, it is also well known that these schemes have accuracy problems in resolving shear layer regions due to excessive numerical dissipation, which occur more seriously in hypersonic flows. Much effort has been put on developing improved FVS-type schemes for high-speed flows, and they have shown reasonable enhancement in accuracy. In contrast, FDS, which exploits the solution of the local Riemann problem, usually provides accurate solutions.

Roe’s FDS<sup>7</sup> has a matrix that becomes zero at a sonic transition point and a contact discontinuity. Thus it is able to capture a shock and resolve the shear layer region very accurately. Unfortunately, it has several robustness problems such as the violation of the entropy condition, failure of local linearization, and appearance of carbuncles<sup>11</sup>. Those defects become more serious in hypersonic flow than in subsonic or supersonic flow.

Although an entropy fix may enhance the robustness, a large amount of entropy fix is usually required in hypersonic flow, which requires extra numerical dissipation. This also may cause a decrease of the total enthalpy behind a shock wave and the inaccurate estimation of the surface-heating rate. Determining the optimal amount of entropy fix without compromising accuracy is difficult and depends highly on the user’s experience. Some variants of Roe’s FDS such

as Harten–Lax–van Leer’s (HLLE) increase the robustness of Roe’s FDS at the expense of accuracy. Therefore, contemporary concern is shifted toward combining the accuracy of FDS and the robustness of FVS. In an effort to design a numerical scheme to meet this concern, the AUSM<sup>6</sup> (advection upstream splitting method) was proposed by Liou and Steffen. Earlier versions of AUSM scheme suffered various limitations. In 2006, Liou proposed and implemented AUSM+-UP-based all-speed formulation<sup>8</sup> for Euler equation. In this work, an attempt was made to extend it to 2-D, axisymmetric and 3-D flows.

3.3.2 AUSM+-UP Scheme

In any AUSM scheme, the inviscid flux is explicitly split into two parts i.e. convective and pressure terms by considering convective and acoustic waves as two physically distinct processes.

$$F = F(c) + P \tag{15}$$

where

$$F^{(c)} = Ma \begin{bmatrix} \rho \\ \rho u \\ \rho h_t \end{bmatrix} \text{ and } P = \begin{bmatrix} 0 \\ p \\ 0 \end{bmatrix}$$

Here the convective flux  $F^{(c)}$  is expressed in terms of the convective speed  $M$  and the passive scalar quantities indicated in the brackets. The pressure flux  $P$  contains nothing but the pressure. Numerical flux  $f_{i+1/2}$  can be expressed as the sum of the numerical convective flux  $f_{i+1/2}^{(c)}$  and the numerical pressure flux  $p_{i+1/2}$ , at the interface  $i+1/2$  straddling the  $i^{\text{th}}$  and the  $i+1^{\text{th}}$  cells.

$$f_{i+1/2} = f_{i+1/2}^{(c)} + p_{i+1/2}, \text{ where one can further write}$$

$$f_{i+1/2}^{(c)} = m_{i+1/2} \Phi_{i+1/2} \text{ and } P_{i+1/2} = \begin{bmatrix} 0 \\ p_{i+1/2} \\ 0 \end{bmatrix}$$

In AUSM+-UP scheme, the interface fluxes are calculated based on the sign of the interface mass flow rate and pressure (evaluated using polynomial Fit)<sup>8</sup>. The flow chart

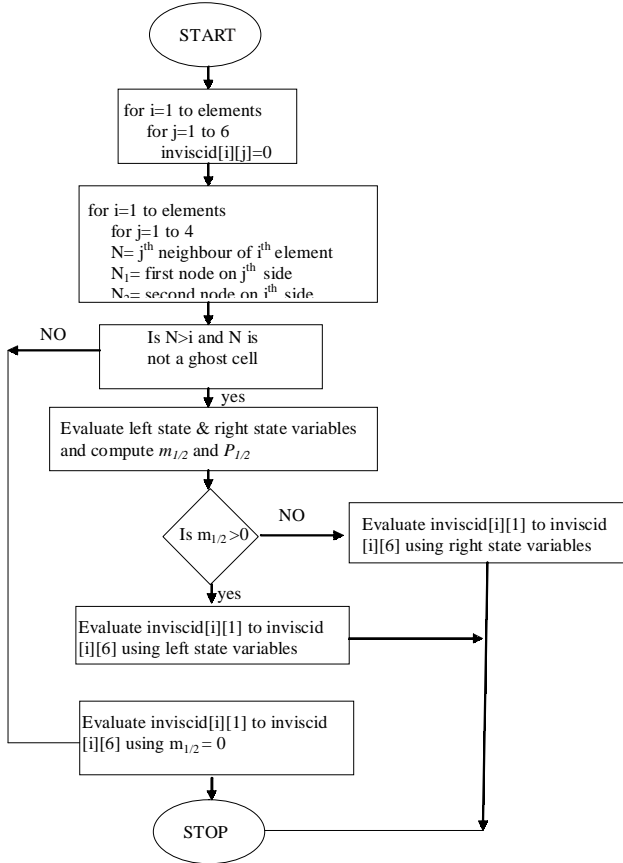


**Figure 2. Flow chart for inviscid flux evaluation using AUSM+UP.**

showing various steps in the implementation of this scheme is given in Fig. 2.

### 3.4 Higher-order Accurate Reconstruction Schemes

Higher-order accurate reconstruction schemes are getting much popularity in computations of high speed compressible fluid flows. Though this method is well developed for structured meshes, higher order reconstruction schemes are rarely used in unstructured meshes, as this procedure is complicated. The presence of spurious oscillations near the discontinuities is the major drawback of higher-order schemes. First-order schemes are free from these oscillations<sup>10,11</sup> but are highly diffusive, and hence, fails to capture the discontinuities with reasonable accuracy. Earlier developments were based on Godunov's theorem. It was based on linear discretization of governing equations. These monotone schemes admit only non-oscillatory solutions that can be at the most first-order accurate. These methods fail if one introduces nonlinearity into the discretisation procedure.

Majority of the published work in this area was based on total variation diminishing (TVD) method or uniformly higher order accurate non-oscillatory (UNO) scheme. Total variation diminishing schemes generally switch to first-order near discontinuities, resulting in local excessive numerical dissipation. In addition, use of flux limiters lead to loss of accuracy, near discontinuities and extrema. On the other hand, UNO schemes overcome these problems<sup>12</sup> to certain

extent but introduce controlled oscillations. In addition to the above issues, the implementation of TVD and UNO in unstructured solvers is difficult and their computational efficiency is not very high.

It has been reported<sup>13</sup> that least square-based derivative evaluation provides much more reliable results. This, in fact, was one of the motivating factor for selecting least square-based approach for reconstruction.

The reconstructing polynomial  $P(\Delta x_i, \Delta y_i)$  used in the solver can be expressed as

$$\begin{aligned}
 P(\Delta x_i, \Delta y_i) = & \phi|_{x_i, y_i} + A_1 \frac{\partial \phi}{\partial x} \Big|_{x_i, y_i} + A_2 \frac{\partial \phi}{\partial y} \Big|_{x_i, y_i} + B_1 \frac{\partial^2 \phi}{\partial x^2} \Big|_{x_i, y_i} + B_2 \frac{\partial^2 \phi}{\partial x \partial y} \Big|_{x_i, y_i} + B_3 \frac{\partial^2 \phi}{\partial y^2} \Big|_{x_i, y_i} + C_1 \frac{\partial^3 \phi}{\partial x^3} \Big|_{x_i, y_i} + C_2 \frac{\partial^3 \phi}{\partial x^2 \partial y} \Big|_{x_i, y_i} \\
 & + C_3 \frac{\partial^3 \phi}{\partial x \partial y^2} \Big|_{x_i, y_i} + C_4 \frac{\partial^3 \phi}{\partial y^3} \Big|_{x_i, y_i} + D_1 \frac{\partial^4 \phi}{\partial x^4} \Big|_{x_i, y_i} + D_2 \frac{\partial^4 \phi}{\partial x^3 \partial y} \Big|_{x_i, y_i} + D_3 \frac{\partial^4 \phi}{\partial x^2 \partial y^2} \Big|_{x_i, y_i} + D_4 \frac{\partial^4 \phi}{\partial x \partial y^3} \Big|_{x_i, y_i} + D_5 \frac{\partial^4 \phi}{\partial y^4} \Big|_{x_i, y_i}
 \end{aligned} \quad (16)$$

Applying least square principle, the above set of equations can also be written in the matrix form as

$$[A_{ij}] [\Delta \phi] = [A_i \phi_j] \quad (17)$$

where the matrices are given in the grey box on the next page.

Evaluate the above coefficients, substitute in Eqn (17) and use any standard numerical technique to get the various derivatives of  $\phi$ . Geometric weights or the solution independent weights are evaluated based on the distance between the control volume  $i$  under consideration and the neighbouring control volume  $j$  is given by

$$\omega_{ij} = \frac{1}{\Delta x_{ji}^2 + \Delta y_{ji}^2} \quad (18)$$

Use of solution weights eliminates the flux limiters from the formulation. However there must be some minimum number of neighbouring control volumes in the stencil depending upon order of accuracy (and hence the order of the matrix). If this number falls below the required number, solver locally creates a new stencil for the control volume  $i$  under consideration to get minimum required neighbours to solve the matrix.

## 4. NUMERICAL SIMULATION

### 4.1 Boundary Conditions

The following boundary conditions<sup>3,4</sup> were used in the analysis.

- *Supersonic inflow*: Static pressure  $P$ , static temperature  $T$  and free stream Mach number  $M\infty$  were specified at this boundary. Other variables are evaluated from local isentropic relations.
- *Supersonic outflow*: Since the flow at the exit of the nozzle is supersonic, the properties ( static pressure, static temperature and velocities ) are linearly interpolated at the exit nodes.
- *Wall boundary (No slip condition)*: Adiabatic no slip conditions were used at solid wall, as this is the numerical boundary of viscous flows.

$$u = v = w = 0, \quad \frac{\partial T}{\partial n} = 0$$

$$\begin{aligned}
 [A_{ij}] &= \begin{bmatrix}
 1 & 0 & 0 & \frac{1}{2}x^2 & -xy & \frac{1}{2}y^2 & \frac{1}{6}x^3 & \frac{1}{2}x^2y & \frac{1}{2}xy^2 & \frac{1}{6}y^3 & \frac{1}{24}x^4 & \frac{1}{6}x^3y & \frac{1}{4}x^2y^2 & \frac{1}{6}xy^3 & \frac{1}{6}y^4 & \dots \\
 \sum_{j=1}^N A_1(A_1A_j) & \sum_{j=1}^N (A_1A_j) & \sum_{j=1}^N (A_1A_j) & \sum_{j=1}^N (A_1B_1) & \sum_{j=1}^N (A_1B_1) & \sum_{j=1}^N (A_1B_1) & \sum_{j=1}^N (A_1C_1) & \sum_{j=1}^N (A_1C_1) & \sum_{j=1}^N (A_1C_1) & \sum_{j=1}^N (A_1C_1) & \sum_{j=1}^N (A_1D_1) & \dots \\
 \sum_{j=1}^N A_2(A_1A_j) & \sum_{j=1}^N (A_2A_1) & \sum_{j=1}^N (A_2A_1) & \sum_{j=1}^N (A_2B_1) & \sum_{j=1}^N (A_2B_1) & \sum_{j=1}^N (A_2B_1) & \sum_{j=1}^N (A_2C_1) & \sum_{j=1}^N (A_2C_1) & \sum_{j=1}^N (A_2C_1) & \sum_{j=1}^N (A_2C_1) & \sum_{j=1}^N (A_2D_1) & \dots \\
 \sum_{j=1}^N B_1(A_1A_j) & \sum_{j=1}^N (B_1A_1) & \sum_{j=1}^N (B_1A_1) & \sum_{j=1}^N (B_1B_1) & \sum_{j=1}^N (B_1B_1) & \sum_{j=1}^N (B_1B_1) & \sum_{j=1}^N (B_1C_1) & \sum_{j=1}^N (B_1C_1) & \sum_{j=1}^N (B_1C_1) & \sum_{j=1}^N (B_1C_1) & \sum_{j=1}^N (B_1D_1) & \dots \\
 \sum_{j=1}^N B_2(A_1A_j) & \sum_{j=1}^N (B_2A_1) & \sum_{j=1}^N (B_2A_1) & \sum_{j=1}^N (B_2B_1) & \sum_{j=1}^N (B_2B_1) & \sum_{j=1}^N (B_2B_1) & \sum_{j=1}^N (B_2C_1) & \sum_{j=1}^N (B_2C_1) & \sum_{j=1}^N (B_2C_1) & \sum_{j=1}^N (B_2C_1) & \sum_{j=1}^N (B_2D_1) & \dots \\
 \sum_{j=1}^N B_3(A_1A_j) & \sum_{j=1}^N (B_3A_1) & \sum_{j=1}^N (B_3A_1) & \sum_{j=1}^N (B_3B_1) & \sum_{j=1}^N (B_3B_1) & \sum_{j=1}^N (B_3B_1) & \sum_{j=1}^N (B_3C_1) & \sum_{j=1}^N (B_3C_1) & \sum_{j=1}^N (B_3C_1) & \sum_{j=1}^N (B_3C_1) & \sum_{j=1}^N (B_3D_1) & \dots \\
 \sum_{j=1}^N C_1(A_1A_j) & \sum_{j=1}^N (C_1A_1) & \sum_{j=1}^N (C_1A_1) & \sum_{j=1}^N (C_1B_1) & \sum_{j=1}^N (C_1B_1) & \sum_{j=1}^N (C_1B_1) & \sum_{j=1}^N (C_1C_1) & \sum_{j=1}^N (C_1C_1) & \sum_{j=1}^N (C_1C_1) & \sum_{j=1}^N (C_1C_1) & \sum_{j=1}^N (C_1D_1) & \dots \\
 \sum_{j=1}^N C_2(A_1A_j) & \sum_{j=1}^N (C_2A_1) & \sum_{j=1}^N (C_2A_1) & \sum_{j=1}^N (C_2B_1) & \sum_{j=1}^N (C_2B_1) & \sum_{j=1}^N (C_2B_1) & \sum_{j=1}^N (C_2C_1) & \sum_{j=1}^N (C_2C_1) & \sum_{j=1}^N (C_2C_1) & \sum_{j=1}^N (C_2C_1) & \sum_{j=1}^N (C_2D_1) & \dots \\
 \sum_{j=1}^N C_3(A_1A_j) & \sum_{j=1}^N (C_3A_1) & \sum_{j=1}^N (C_3A_1) & \sum_{j=1}^N (C_3B_1) & \sum_{j=1}^N (C_3B_1) & \sum_{j=1}^N (C_3B_1) & \sum_{j=1}^N (C_3C_1) & \sum_{j=1}^N (C_3C_1) & \sum_{j=1}^N (C_3C_1) & \sum_{j=1}^N (C_3C_1) & \sum_{j=1}^N (C_3D_1) & \dots \\
 \sum_{j=1}^N C_4(A_1A_j) & \sum_{j=1}^N (C_4A_1) & \sum_{j=1}^N (C_4A_1) & \sum_{j=1}^N (C_4B_1) & \sum_{j=1}^N (C_4B_1) & \sum_{j=1}^N (C_4B_1) & \sum_{j=1}^N (C_4C_1) & \sum_{j=1}^N (C_4C_1) & \sum_{j=1}^N (C_4C_1) & \sum_{j=1}^N (C_4C_1) & \sum_{j=1}^N (C_4D_1) & \dots \\
 \sum_{j=1}^N D_1(A_1A_j) & \sum_{j=1}^N (D_1A_1) & \sum_{j=1}^N (D_1A_1) & \sum_{j=1}^N (D_1B_1) & \sum_{j=1}^N (D_1B_1) & \sum_{j=1}^N (D_1B_1) & \sum_{j=1}^N (D_1C_1) & \sum_{j=1}^N (D_1C_1) & \sum_{j=1}^N (D_1C_1) & \sum_{j=1}^N (D_1C_1) & \sum_{j=1}^N (D_1D_1) & \dots \\
 \sum_{j=1}^N D_2(A_1A_j) & \sum_{j=1}^N (D_2A_1) & \sum_{j=1}^N (D_2A_1) & \sum_{j=1}^N (D_2B_1) & \sum_{j=1}^N (D_2B_1) & \sum_{j=1}^N (D_2B_1) & \sum_{j=1}^N (D_2C_1) & \sum_{j=1}^N (D_2C_1) & \sum_{j=1}^N (D_2C_1) & \sum_{j=1}^N (D_2C_1) & \sum_{j=1}^N (D_2D_1) & \dots \\
 \sum_{j=1}^N D_3(A_1A_j) & \sum_{j=1}^N (D_3A_1) & \sum_{j=1}^N (D_3A_1) & \sum_{j=1}^N (D_3B_1) & \sum_{j=1}^N (D_3B_1) & \sum_{j=1}^N (D_3B_1) & \sum_{j=1}^N (D_3C_1) & \sum_{j=1}^N (D_3C_1) & \sum_{j=1}^N (D_3C_1) & \sum_{j=1}^N (D_3C_1) & \sum_{j=1}^N (D_3D_1) & \dots \\
 \sum_{j=1}^N D_4(A_1A_j) & \sum_{j=1}^N (D_4A_1) & \sum_{j=1}^N (D_4A_1) & \sum_{j=1}^N (D_4B_1) & \sum_{j=1}^N (D_4B_1) & \sum_{j=1}^N (D_4B_1) & \sum_{j=1}^N (D_4C_1) & \sum_{j=1}^N (D_4C_1) & \sum_{j=1}^N (D_4C_1) & \sum_{j=1}^N (D_4C_1) & \sum_{j=1}^N (D_4D_1) & \dots \\
 \sum_{j=1}^N D_5(A_1A_j) & \sum_{j=1}^N (D_5A_1) & \sum_{j=1}^N (D_5A_1) & \sum_{j=1}^N (D_5B_1) & \sum_{j=1}^N (D_5B_1) & \sum_{j=1}^N (D_5B_1) & \sum_{j=1}^N (D_5C_1) & \sum_{j=1}^N (D_5C_1) & \sum_{j=1}^N (D_5C_1) & \sum_{j=1}^N (D_5C_1) & \sum_{j=1}^N (D_5D_1) & \dots
 \end{bmatrix} \\
 [\Delta\phi] &= \begin{bmatrix}
 \phi_i & \frac{\partial\phi_i}{\partial x} & \frac{\partial\phi_i}{\partial y} & \frac{\partial^2\phi_i}{\partial x^2} & \frac{\partial^2\phi_i}{\partial x\partial y} & \frac{\partial^2\phi_i}{\partial y^2} & \frac{\partial^3\phi_i}{\partial x^3} & \frac{\partial^3\phi_i}{\partial x^2\partial y} & \frac{\partial^3\phi_i}{\partial x\partial y^2} & \frac{\partial^3\phi_i}{\partial y^3} & \frac{\partial^4\phi_i}{\partial x^4} & \frac{\partial^4\phi_i}{\partial x^3\partial y} & \frac{\partial^4\phi_i}{\partial x^2\partial y^2} & \frac{\partial^4\phi_i}{\partial x\partial y^3} & \frac{\partial^4\phi_i}{\partial y^4} & \dots
 \end{bmatrix}^T \\
 [A_i\phi_j] &= \begin{bmatrix}
 \phi_i & \sum_{j=1}^N A_1\phi_j & \sum_{j=1}^N A_2\phi_j & \sum_{j=1}^N B_1\phi_j & \sum_{j=1}^N B_2\phi_j & \sum_{j=1}^N B_3\phi_j & \sum_{j=1}^N C_1\phi_j & \sum_{j=1}^N C_2\phi_j & \sum_{j=1}^N C_3\phi_j & \sum_{j=1}^N C_4\phi_j & \sum_{j=1}^N D_1\phi_j & \sum_{j=1}^N D_2\phi_j & \sum_{j=1}^N D_3\phi_j & \sum_{j=1}^N D_4\phi_j & \sum_{j=1}^N D_5\phi_j & \dots
 \end{bmatrix}^T
 \end{aligned}$$

- **Subsonic inflow:** Stagnation conditions of pressure  $P_0$  and temperatures  $T_0$  were specified at this boundary. Other variables were evaluated from local isentropic relations. This procedure allows for the influence of downstream flow at the subsonic inflow. Here pressure is extrapolated and not the velocity because forcing the direction of inflow provides better convergence. If velocity is extrapolated, then in some cases, the velocity vector may be in reverse direction for certain initialization and can lead to physically unacceptable solutions.

**4.2 Analysis Procedure**

Analysis has been carried out using in-house solver, which has been validated for different flow regimes. Computational domains were modeled using IDEAS software and filled with hexahedron and quadrilaterals grids (using Hypermesh) for 3-D and 2-D simulations, respectively and initialised with appropriate flow parameters. Post-processing was done using Hypermesh software

**5. SOLVER VALIDATION**

Various schemes and models were validated by carrying out numerical experiments in a systematic manner as explained below:

- (i) Hypersonic flow over blunted cone flare to validate finite volume formulation, viscous flux evaluation, AUSM++UP scheme, reconstruction scheme and stencil generating algorithms. The flow is laminar and hence eliminates

- uncertainty due to turbulence.
- (ii) Supersonic flow inside NASA B2 nozzle to validate turbulence model and capability of solver to simulate flows inside a C-D nozzle.
- (iii) Film cooling for a typical reentry module to validate the solver for both structured and unstructured grids as well as for normal jet injection scenario experienced inside turbine start-up system.
- (iv) Flow inside a typical high altitude test facility to demonstrate the capability of the solver in capturing multiple shocks, which also exist in case of turbine start-up system.

**5.1 Hypersonic Flow Over Blunted Cone-flare**

Flow field around blunted cone-flare is of particular interest since it features most of the aspects of the hypersonic flow around re-entry vehicles. The region between the cone and the flare is critical wrt the evaluation of the surface heat flux. Flow separation is induced by the shock wave-boundary layer interactions (Fig. 3), with subsequent flow reattachment that can dramatically enhance the surface heat transfer. The experiment was carried out in H3 hypersonic wind tunnel<sup>14</sup> and the chamber conditions ensure that the flow is purely laminar. Hence this is one of the most suited test cases for validating various schemes of the solver since uncertainties due to turbulence are eliminated.

**Computational Domain And Flow Conditions**

The geometry and computational domain of the blunted

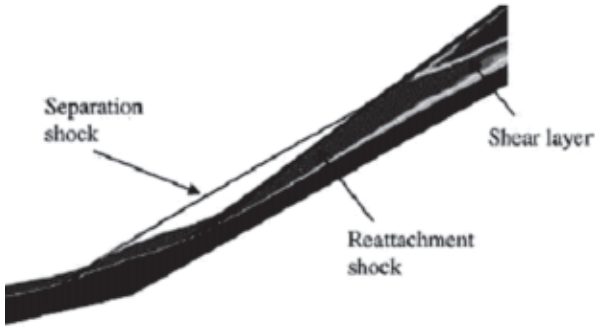


Figure 3. Flow features near flare-cone junction in hypersonic flow.

cone-flare is shown in Fig 4. Air at 580 K and 32 bar is passed through an axisymmetric nozzle where it expands to a nominal Mach number of 6 and enters the test section. The stagnation pressure is 10 bar and the unit length Reynolds number is  $8 \times 10^6 \text{ m}^{-1}$ . Under these conditions, flow over the entire blunted cone-flare is laminar.

Figure 5 shows the various computational grids used for simulations. Simulations were carried out using constant wall temperature of 300 K. Grid independent solutions were obtained for  $2800 \times 140$  grids. The comparison of computed wall pressure distribution with experiment for different grids is shown in Fig. 6. Coarse mesh is not capable of capturing

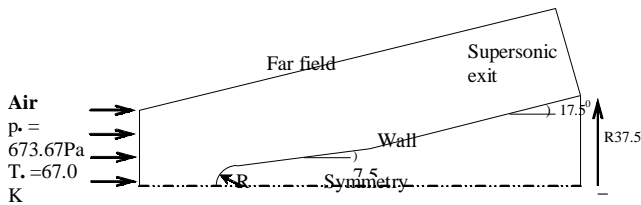


Figure 4. Geometry and boundary conditions for hypersonic flow simulation.

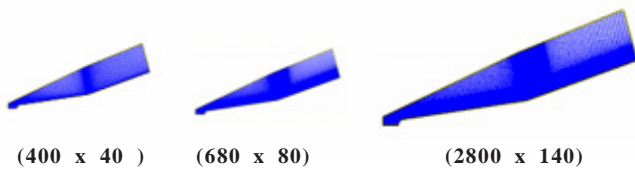


Figure 5. Computational grids for blunted cone-flare.

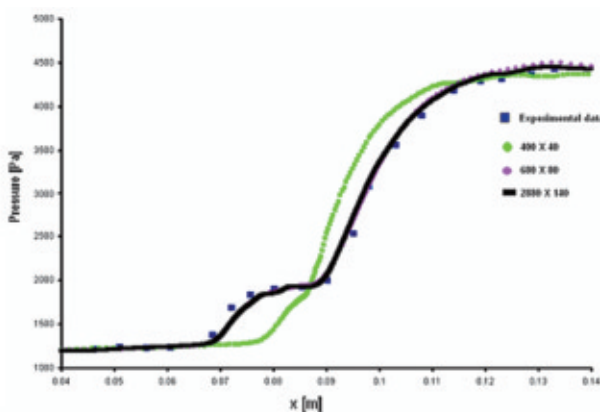


Figure 6. Comparison of wall pressure distribution.

the separation region in the cone-flare junction exactly. Refined mesh successfully predicts the wall pressure in all regions. The vector plot shown in Fig. 7 gives the nature of recirculation region in cone-flare junction. Mach number contour plot corresponding to finest grid is shown in Fig. 8. All features such as detached bow shock in stagnation region and shock-boundary layer interaction in cone-flare junction are captured.

### 5.2 NASA B<sub>2</sub> nozzle

A two-dimensional flow field simulation was carried for NASA B<sub>2</sub> nozzle<sup>15</sup> shown in Fig 9. This nozzle is a standard facility nozzle used to supply supersonic flow at Mach 2 to various test facilities.

Simulations were carried out using subsonic boundary conditions at inlet. Top wall is a no-slip wall and a supersonic condition is maintained at exit. Figure 10 gives the various grids used for grid-independence studies. Figure 11 gives the wall pressure distribution for various grids. Grid-independent solution was obtained for  $108 \times 40$  grids. The solver could predict the pressure distribution inside the nozzle with reasonable accuracy. Figure 12 gives the Mach contours and it is evident that all flow features within a C-D nozzle have been established with reasonable accuracy. The predicted nozzle exit Mach number of 2.02 at the centre is in line with the design value.

### 5.3 Film Cooling for a re-entry Module

A numerical simulation of film cooling for re-entry module is presented. Simulation has been carried out for a simple axisymmetric re-entry module with and without film cooling. Important features of the flow field resulting due to counter flow injection in a sphere-cone-flare, and are shown in Fig. 13. The counter flow jet separates from the sharp-edged orifice. The jet expands till a Mach disc is formed, and thereafter, it turns in the direction of mainstream. Due to the low pressure created by expansion of the jet, a recirculation region is formed in the shear layer. The jet layer mixes with shear layer of mainstream only after this recirculation region thereby forming a dividing stream surface. The jet layer turns along the body surface flows along downstream. Experimental results of Aso, *et al.*<sup>16</sup> on opposing jet in hypersonic flow are used to validate the present code. Sonic nitrogen injection is introduced through a hole of 4 mm dia in the opposite direction of supersonic free stream ( $M = 3.96$ ). The diameter of the blunt model is 50 mm and the Reynolds number based on this diameter of blunt body is  $2.1 \times 10^6$ . Total pressure ratio of jet to free stream is maintained as 0.276. The computational domain and test conditions are summarised in Fig. 14.

The computational domain is discretised into 118800 control volumes with two sets of grid blocks. A fine block of grid introduced near the wall extends 20 mm above wall. Minimum grid size near the wall is 0.01 mm. A supersonic inflow condition was maintained at the left face and outflow condition was maintained at the right face of the computational domain. No-slip wall condition is given for blunt body wall

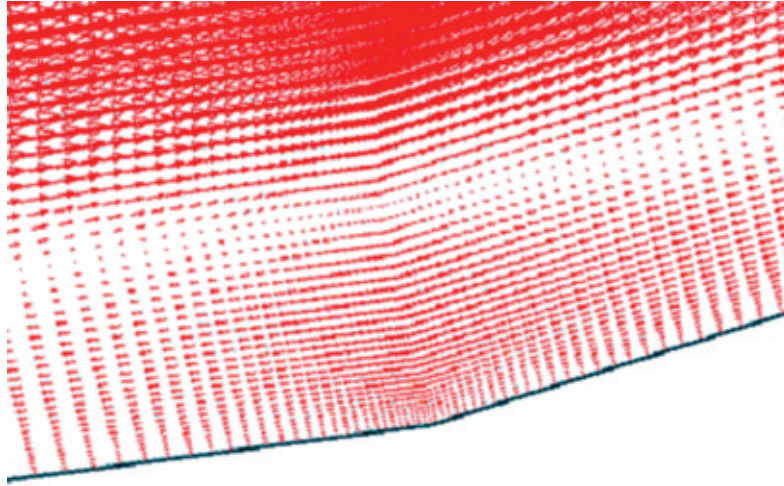


Figure 7. Recirculation zone near cone-flare junction.

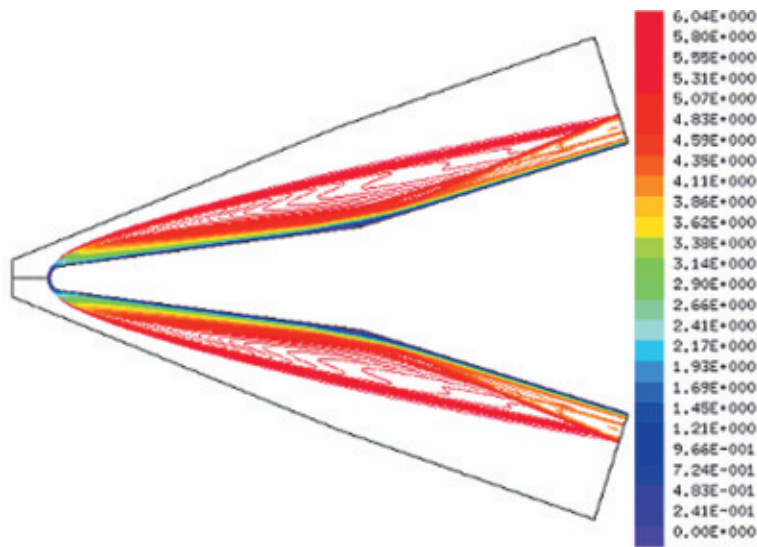


Figure 8. Mach contour plot for blunted cone-flare.

except at portion of jet, where jet is introduced as a constant velocity condition. Entire flow field is initialised with the free stream condition.

Mach number contour plot of the computed results is shown in Fig. 15. Most of the features of the flow field resulting due to counter-flow injection in a sphere-cone-flare, illustrated in Fig. 13 have been successfully captured. The formation of Mach disc, recirculation region formed due to expansion of jet, detached shock wave, recompression shock, etc can be visualised in this plot. Computation of another test on the same blunt body without injection is

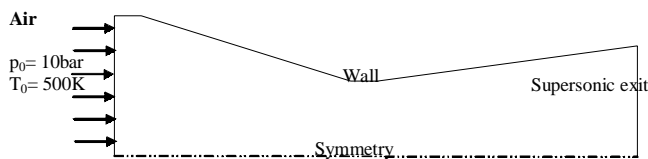


Figure 9. Geometry and boundary conditions for B<sub>2</sub> nozzle simulation.

done to show the effect of gas jet on aerodynamic heating. Mach number contour plot of this computed result is shown in Fig. 15. Experimental data for wall pressure are available for both cases; computed results are compared with it and are shown in Fig. 16. It is evident from the plot that the numerical scheme used is capable of predicting the flow behavior. Computed pressure value near to recirculation region (injection case) deviates slightly due to the presence of associated unsteadiness. Also numerical result of Aso, *et al.*<sup>27</sup> has also a similar trend for the pressure variation. Pressure reduction on nose of blunt body resulting due to introduction of jet can also be observed.

To study the performance and accuracy of the solver for structured and unstructured grids, 118800 structured grids and 100499 unstructured grids were considered (Fig. 17) for simulation. Figure 18 shows the comparison of experimental and numerical wall pressure distribution for these 2 grids. It is clear that solver gives reasonable accuracy for both structured and unstructured grids.

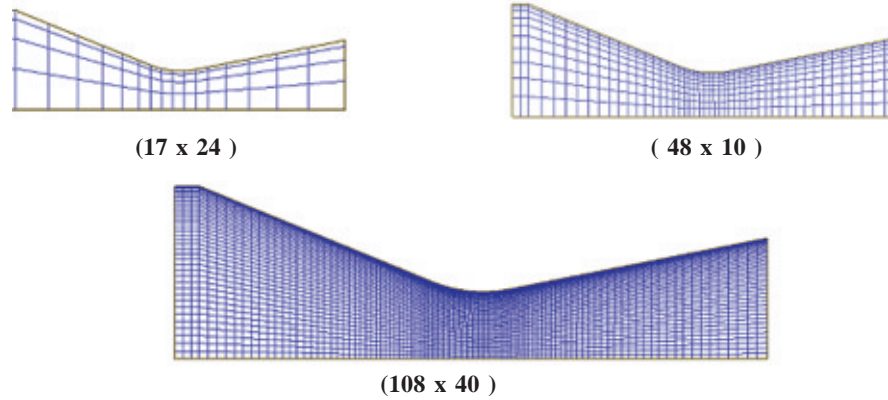


Figure 10. Computational grids for NASA B<sub>2</sub> nozzle.

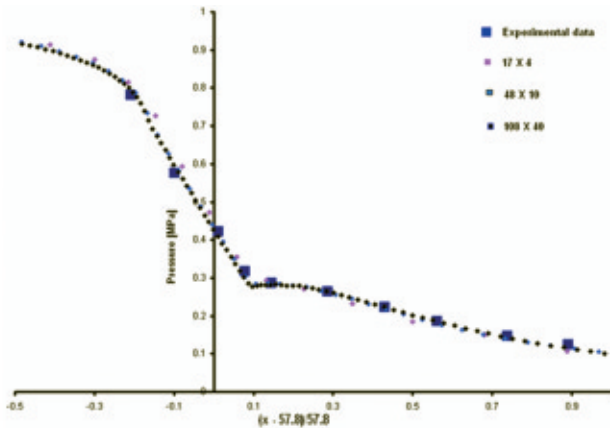


Figure 11. Grid convergence study-wall pressure distribution.

#### 5.4 Flow with Multiple Shocks Inside a High Altitude Test Facility

A 2-D flow field simulation was carried out for a high altitude test facility<sup>17</sup> (shown in Fig 19). The test motor was attached to the test facility having convergent-divergent nozzle, which accelerates flow to high supersonic velocity. This flow was directed to a diffuser through a constant

area duct. The entire test facility geometry generates multiple shocks within the domain and simulation of such a flow is challenging task. Simulation was carried out using Goldberg’s one equation turbulence model and grid independence solution was obtained for 116800 grids (shown in Fig. 20).

Figure 21 shows the Mach contour inside the computational domain. We can see that the flow accelerates to Mach 5.0 in the facility nozzle and then series of shock waves are formed in the constant area region. Finally it gets accelerated in the divergent region. Fig. 22 presents the variation of static pressure with axial distance from nozzle throat. The simulation has captured multiple shocks and wall static pressure matches with the experimental data with slight deviations at some points, which is probably due to unaccounting of the property variations.

### 6. NUMERICAL SIMULATION OF FLOW IN TURBINE STARTUP SYSTEM

#### 6.1 Prediction of Flow in Solid Motor and the C-D Nozzle

The spinner motor used in a typical turbine startup system consists of a solid propellant capable of supplying

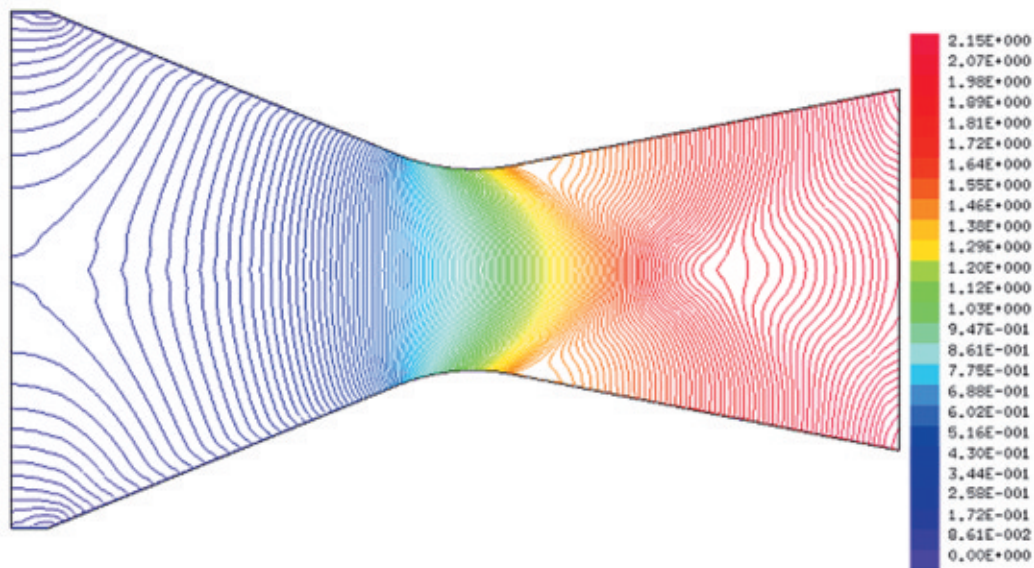


Figure 12. Mach number contours inside B<sub>2</sub> nozzle.

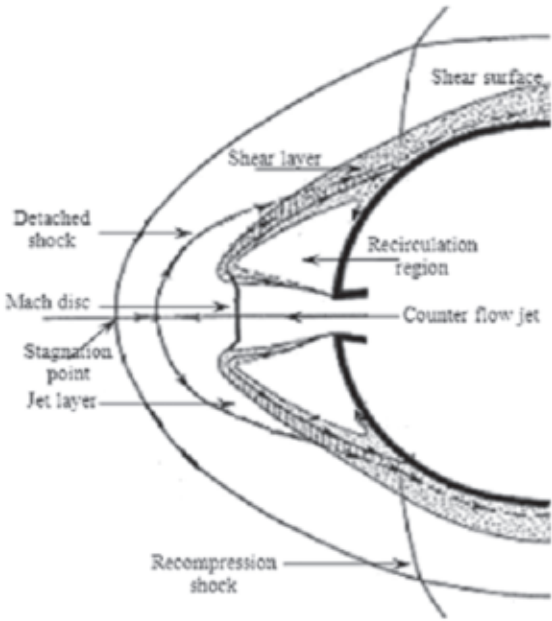


Figure 13. Flow Physics of Film Cooling.

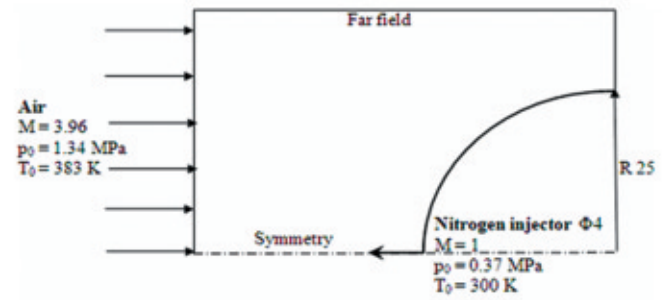


Figure 14. Computational domain and test conditions.

required amount of combustion products (minimum particulates) at a given operating temperature. Theoretical flame temperature for the spinner motor can be obtained using the equilibrium composition analysis (CEA code<sup>18</sup>). During the test, the most common doubt raised by the experimentalists is whether a temperature probe kept in the flow measures static or stagnation value. The answer to this can be obtained by simulating the flow scenario<sup>18</sup> with the temperature probe placed in the flow as shown

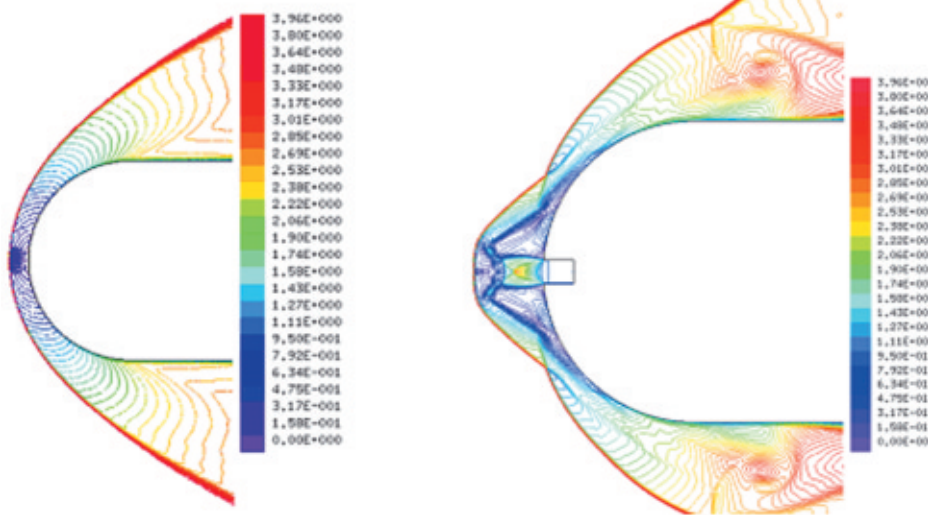


Figure 15. Flow Physics of Film Cooling.

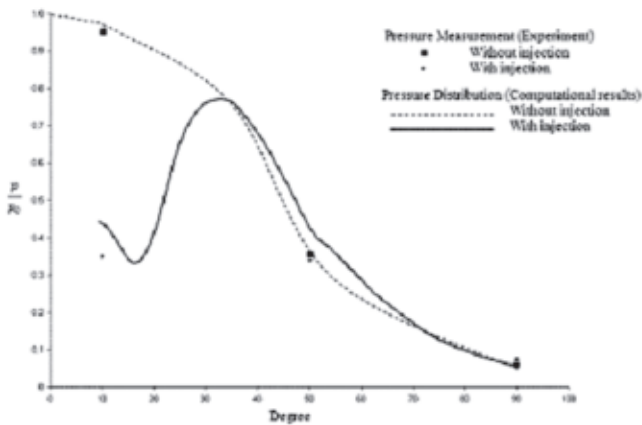


Figure 16. Comparison of computed wall pressure distribution with experiment.

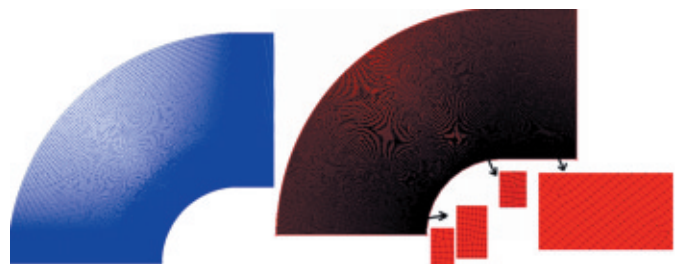


Figure 17. Structured and unstructured grid for re-entry model without film cooling.

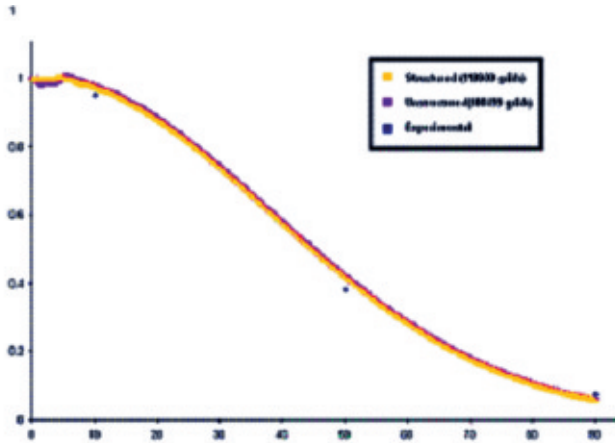


Figure 18. Comparison of numerical and experimental pressure for structured and unstructured grids.



Figure 19. Computational domain for HAT facility.

in Fig. 23. Whenever a probe is placed in a flow, the region close to the probe becomes stagnant and hence the probe measures stagnation temperature. To validate the above predictions, a static test ( $P_0 = 80$  bars,  $T_0 = 1500$  K) was carried out by placing the temperature probe in the supersonic flow regime outside the nozzle ahead of the normal shock as shown in Fig. 24. The measured temperature (1542 K) was close to the simulated value (1500 K).

### 6.2 Integrated Analysis of Solid Motor, C-D Nozzle and Guiding Duct

This analysis was required for designing the guiding duct. Once the space available for the duct and the motor-nozzle assembly was finalised, the only option available to control the combustion gas temperature was to design the duct with appropriate geometry and material. One has to keep in mind the fact that for upper stages of launch vehicle, active cooling methods are not feasible since it results in additional dead weight. The flow and thermal behaviour of the combustion gases in the duct can be studied in two ways. One is to carry out integrated analysis of the motor, nozzle, and the duct, and get the flow and thermal properties at the exit plane of the duct. Another

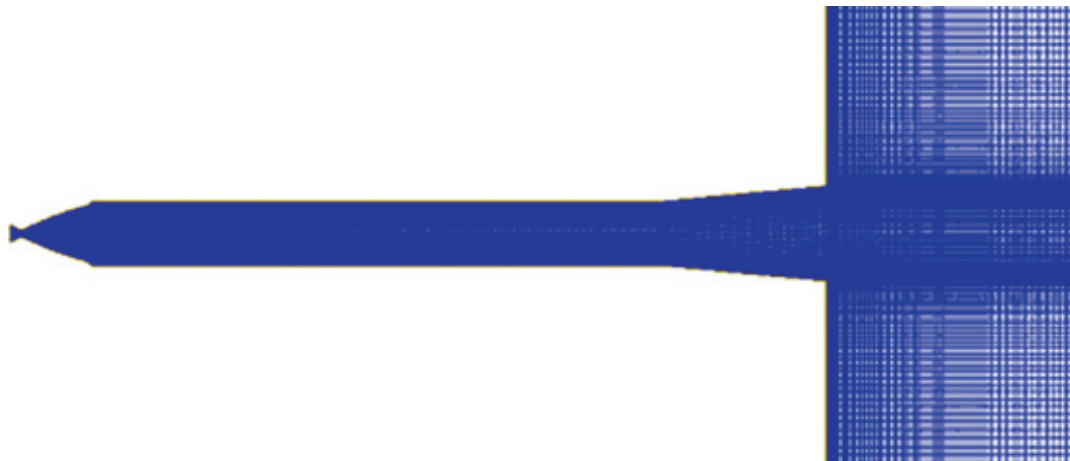


Figure 20. Computational grids (116800) used for HAT facility simulation.



Figure 21. Mach contours inside HAT facility.

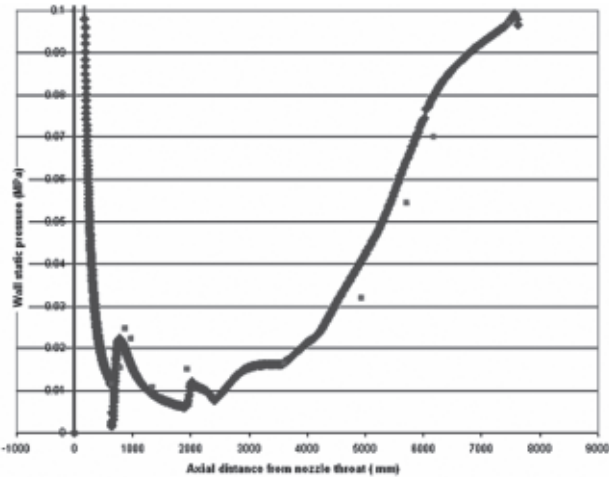


Figure 22. Comparison of experimental and numerical pressure distribution for HAT facility.

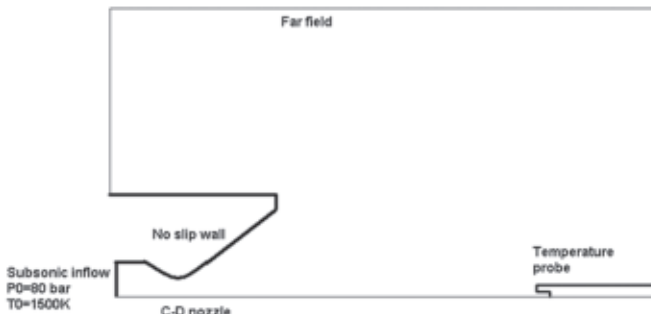


Figure 23. Computational domain.

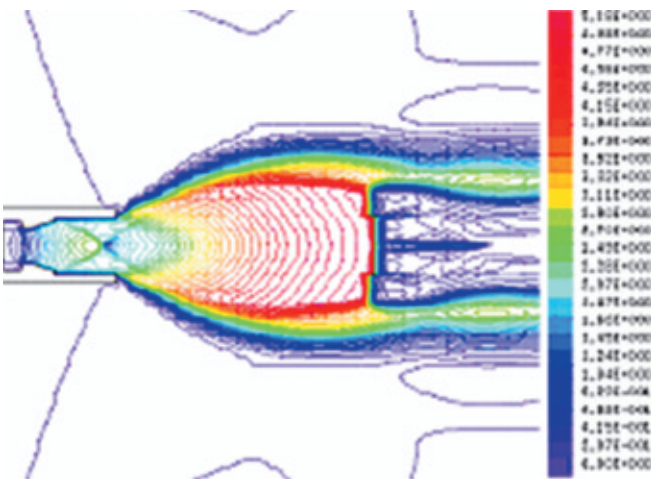


Figure 24. Mach contours showing normal shock location.

way is to get the flow and thermal parameters from the analysis of the motor and the nozzle and explicitly force these conditions at the region where it is connected to the duct. Since the flow at the exit of the nozzle is supersonic, the static pressure, static temperature and the resultant velocity at the duct inlet (injection point) was to be specified.

The heat transfer through the duct material can be addressed in two ways. One method is to carry out a conjugate heat transfer analysis where flow and heat transfer equations are solved simultaneously for multi-block grids.

The second method includes simulating the fluid flow alone assuming that the duct wall is adiabatic and getting the heat transfer coefficient using appropriate correlations and finally evaluating net heat transfer. The first method requires enormous computational time and resources. The second method is simple and straightforward and provides reasonable accuracy required for design phase. Here the second approach is followed for the heat transfer computations.

Figure 25 shows the computational domain and Fig. 26 shows the Mach number distribution within the guiding duct assuming adiabatic wall conditions.

At the exit of the duct, Mach number distribution is asymmetric due to the geometry. More the asymmetry in the exit Mach number, more will be the time required to fill the inlet manifold uniformly, and hence, supply uniform mass flow through each of the guiding nozzles in the inlet manifold. The local convective heat transfer coefficient at different locations in the duct can be evaluated from the flow parameters and by accounting for the radiation loss to the ambient. The net heat transfer from the duct was evaluated considering the convective heat transfer obtained using the flow parameters and the radiation losses<sup>16</sup> to the ambient. The total temperature obtained at the exit of the duct thus provides guidelines for changing the duct geometry and/or material.

### 6.3 Integrated Analysis of Solid Motor, C-D Nozzle, Duct and the Inlet Manifold

Here also, the flow and thermal behaviour of the combustion gases in the duct can be addressed in two ways. One way is to carry out integrated analysis of the motor, nozzle, duct, and inlet manifold with the guiding nozzle to get the flow and thermal properties at the exit of the guiding nozzles. Another way is to get the flow and thermal parameters from the analysis of the motor and the nozzle and explicitly force these conditions at the region where it is connected to the duct. In this integrated analysis, conjugate fluid-heat transfer simulation becomes costly affair and hence fluid flow simulation was used assuming walls to be adiabatic and perform heat transfer computations using appropriate correlations<sup>11</sup>. Figure 27 shows the computational domain for integrated analysis of motor, nozzle, duct, and inlet manifold and Fig 28 shows the computational grid used for simulations.

Figure 29 gives the Mach number distribution at the exit of the duct (inlet of the manifold). The Mach number distribution is not symmetric about the duct axis due to the geometric constraints. This asymmetry prevents uniform filling of the inlet manifold with the combustion gases. One side of the torroid gets more mass flow initially and supplies more combustion gases to the nozzles on that side. This effect is clearly visible in Figs 30 and 31, which give Mach number distribution at the exit of each of the 39 nozzles. Mach number varies from 1.75 to 1.9.

Figure 32 gives the static pressure variation at the exit of the 39 nozzles. However, after a small fraction of time, torroid acts as a reservoir and ensures more or less the

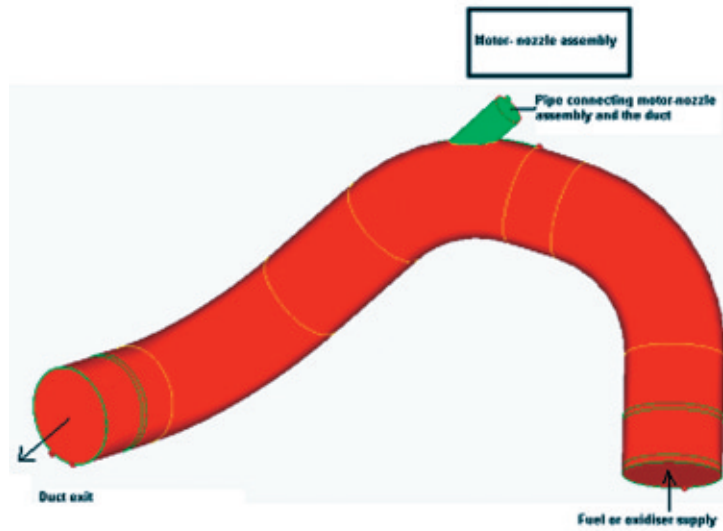


Figure 25. Computational domain for motor-nozzle-duct assembly.

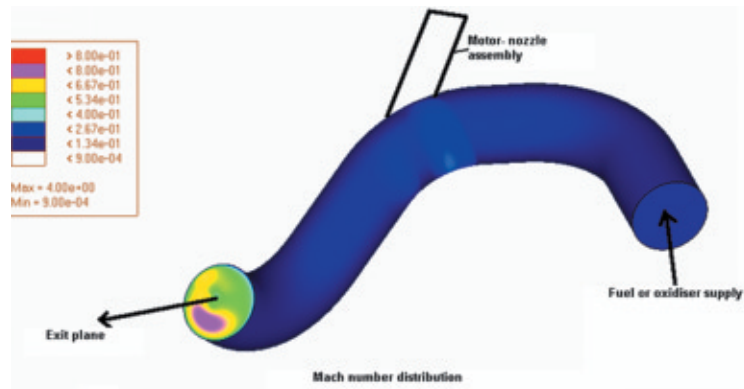


Figure 26. Mach number distribution in the duct.

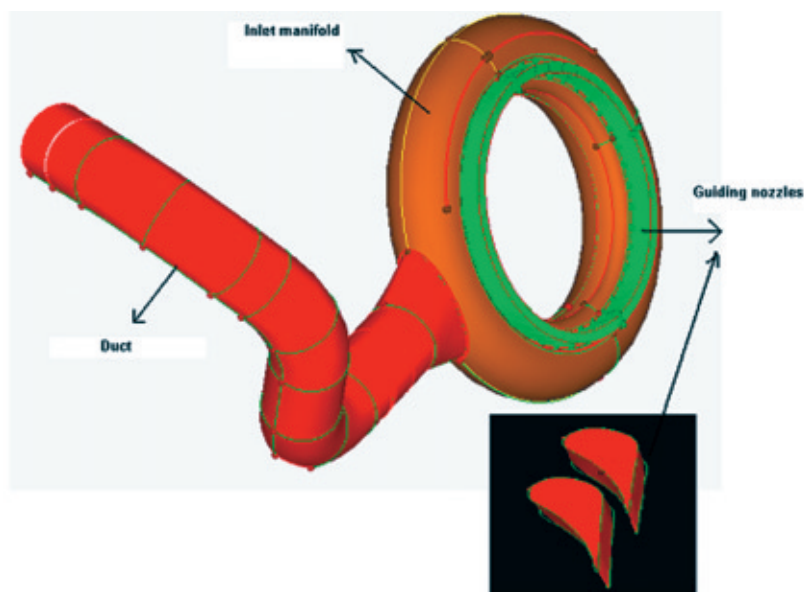


Figure 27. Computational domain for integrated analysis.



Figure 28. Computational grid for integrated analysis.

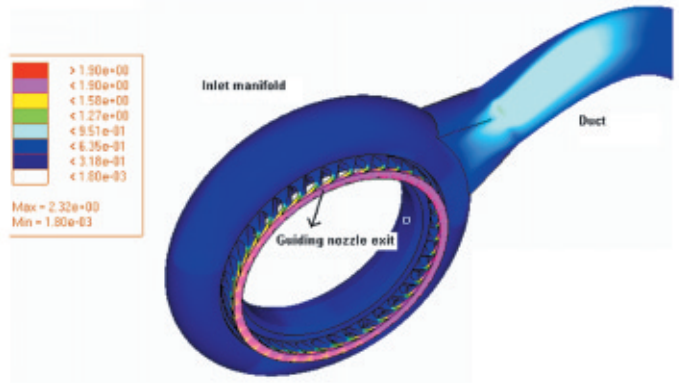


Figure 30. Mach number distribution in the computational domain.

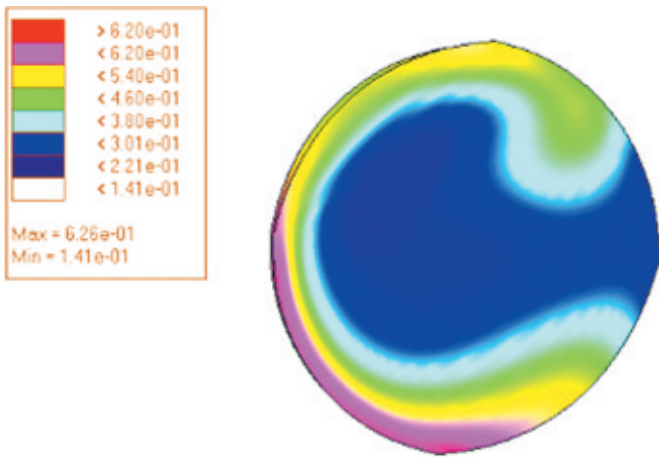


Figure 29. Mach number distribution at the manifold inlet.

same mass flow rate through each of the 39 nozzles. The flow parameters at different locations in the computational domain are used to evaluate the heat transfer coefficients using appropriate correlations. Using these correlations, the heat transfer through the hardware is estimated and finally the temperature at the exit of the nozzle block, where turbine blades are positioned, are obtained. For the given flow conditions, analysis and simple calculations showed that the turbine blades would be subjected to a temperature of about 1000 K, which is within the design specifications.

### 7. CONCLUSION

Unstructured finite volume based higher order accurate flow solver using AUSM+-UP scheme was developed to carry out numerical simulation of high speed flows involving multiple shocks inside a turbine start up system. The solver has been tested for its robustness and accuracy by simulating flow over standard test cases and a reasonably good match has been established between simulated and measured flow parameters. The solver was used to carry out numerical simulations of various components of a turbine startup system in order to eliminate costly static tests of individual

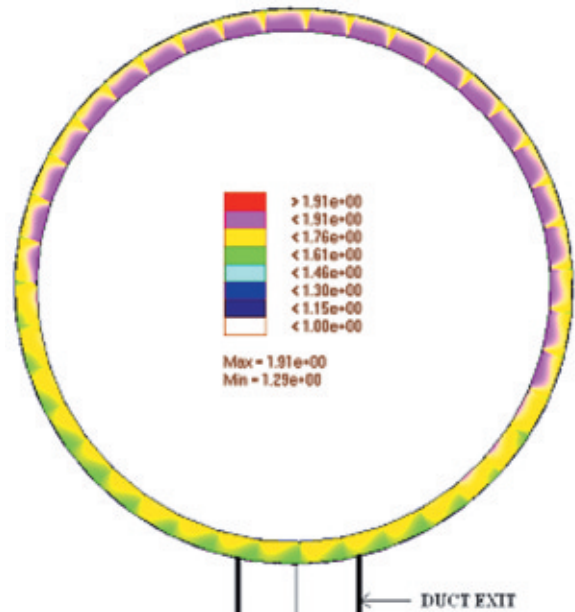


Figure 31. Mach number distribution at the exit of 39 nozzles.

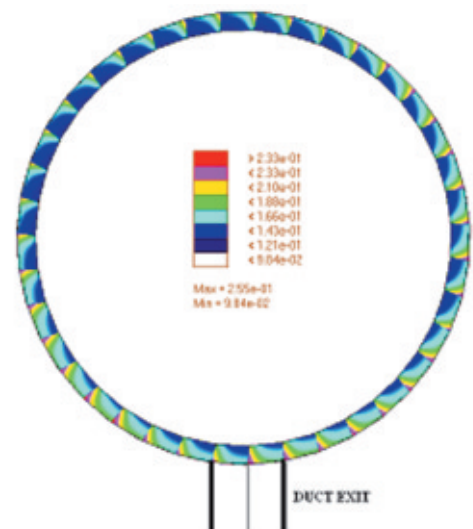


Figure 32. Mach number distribution at the exit of 39 nozzles.

components. Spinner motor and C-D nozzle simulations were carried out to ensure that required amount of combustion products (capable of starting the turbine) are generated at given temperature and pressure. Then the duct was attached to turbine spinner and a CFD simulation was carried out to get the flow parameters within the duct. Using appropriate correlations, net heat transfer through the duct wall was calculated and finally the duct exit conditions were evaluated.

An integrated analysis was carried out with spinner motor, C-D nozzle, duct and inlet manifold to get the flow parameters inside the inlet manifold and the exit of the guiding nozzles. Using appropriate correlations, net heat transfer through all the walls was evaluated. Initially the flow is not symmetric at the duct exit due to geometric constraints and this prevents the torroid from getting uniformly filled with combustion gases. This in turn results in non-uniform mass flow through each of the 39 nozzles. However within a fraction of a second, the torroid gets filled completely and acts a reservoir thereby ensuring uniform mass flow through each of the 39 blades. Flow simulations and simple heat transfer calculations predicted the temperature at the exit of the nozzle block to be of the order of 1000 K, which was in close agreement with the static test measured value of 1123 K.

#### REFERENCES

1. Kuo, K.K. Principles of combustion. John Wiley & Sons, 1986.
2. Stephen, R. Turns, An introduction to combustion. McGraw-Hill, 2000.
3. Dale, A. Anderson. Computational fluid mechanics and heat transfer. McGraw-HILL, 1984.
4. Anderson, John D. Jr. Computational fluid dynamics (The basics with applications). McGraw-HILL 1990.
5. Yakhot, V.; Orzag, A.; Gatski, T.B. & Speziade C.B., Development of turbulence model for shear flows by a double expansion technique, *Physics of Fluids*, 1992, **4**, pp. 1510-20.
6. Meng-Sing Liou, Ten years in the making-AUSM family. NASA/TM-2001-210977. AIAA-2001-2521.
7. Toro, E.F. Riemann solvers and numerical methods for fluid dynamics. 1997.
8. Meng-Sing Liou, A sequel to AUSM, Part II : AUSM+-UP for all speeds. *J. Comput. Phy.* 2006, **214**, 137-70.
9. Meng-Sing Liou. A Sequel to AUSM; AUSM+ *J. Comp. Phy.* 1996, **129**, 364-82.
10. Kim, K.H.; Kim, C. & Rho, O.H. Methods for accurate computations of hypersonic flows: AUSMPW+ Scheme, *J. Comput. Phy.*, 2001, **174**, 38-80.
11. K.H.Kim, C.Kim, O.H Rho, Methods for accurate computations of hypersonic flows: shock aligned grid technique. *J. Comp. Phy.*, 2001, **174**, 81-119.
12. Zingg, D.W. Comparison of several spatial discretizations for the Navier-stokes equations. *J. Comput. Phy.*, 2000, **160**, 120-126.
13. Aftosmis, M.; Gaitonde, D. & Tavares, T.S. Behavior of linear reconstruction techniques on unstructured meshes. *AIAA Journal*, 2005, **33**.
14. Savino, R. & Paterna, D. Blunted cone-flare in hypersonic flow, *Computers and Fluids*, 2005, **34**, pp. 859-75.
15. Mary, L.M.; Lawrence, E.P. & Richard, J.R. The effect of throat contouring on two-dimensional converging-diverging nozzles at static conditions, *NASA TP 1704*.
16. Aso, S.; Hayashi, K. & Mizoguchi, M. A study on aerodynamic heating reduction due to opposing jet in hypersonic flow, *AIAA 2002-0646*.
17. Dileep, K.N & Jayachandran, T. Technical report on high altitude test facility, VSSC/ISRO, 2005.
18. Nair, Praveen; Reddy, Jayabharata & Jayachandran, T. Numerical simulation of turbine spinner plume with stagnation temperature probe. *In International Conference on Recent Advances in Experimental Fluid Mechanics*. Vijayawada, March 2008.